

Resorbable optical fibers for interstitial photodynamic therapy—assessment of photosensitizer spatial distribution in tumors

Original

Resorbable optical fibers for interstitial photodynamic therapy—assessment of photosensitizer spatial distribution in tumors / Talekkara Pandayil, Jawad; Šušnjar, Stefan; Muhammad Daniyal Ghauri, ; Sanathana Konugolu Venkata Sekar, ; Swartling, Johannes; Janner, Davide; Boetti, Nadia G.; Reistad, Nina. - In: JOURNAL OF BIOMEDICAL OPTICS. - ISSN 1560-2281. - 30:5(2025). [10.1117/1.JBO.30.5.058001]

Availability:

This version is available at: 11583/3000876 since: 2025-06-12T20:27:17Z

Publisher:

SPIE

Published

DOI:10.1117/1.JBO.30.5.058001

Terms of use:

This article is made available under terms and conditions as specified in the corresponding bibliographic description in the repository

Publisher copyright

(Article begins on next page)

Resorbable optical fibers for interstitial photodynamic therapy—assessment of photosensitizer spatial distribution in tumors

Jawad T. Pandayil^{1, a, b, †} Stefan Šušnjar^{1, c, d, *, †} Muhammad Daniyal Ghauri^{1, e}
Sanathana Konugolu Venkata Sekar^{1, e, f} Johannes Swartling^{1, d} Davide Janner^{1, b}
Nadia G. Boetti^{1, a} and Nina Reistad^{1, c}

^aFondazione LINKS-Leading Innovation and Knowledge for Society, Torino, Italy

^bPolitecnico di Torino, Dipartimento di Scienza Applicata e Tecnologia (DISAT) and RU INSTM, Torino, Italy

^cLund University, Department of Physics, Lund, Sweden

^dSpectraCure AB, Lund, Sweden

^eTyndall National Institute, Cork, Ireland

^fBioPixS Ltd– Biophotonics Standards, IPIC, Cork, Ireland

ABSTRACT. **Significance:** Optical-quality bioresorbable implants, which gradually dissolve within the body, are gaining increasing interest due to their potential to eliminate the need for revision surgeries. These implants show significant promise in treating deep-seated tumors in high-risk areas, such as the brain, and offer extended capabilities for monitoring interstitial physiological parameters or pharmacokinetics through photonic technologies.

Aim: A proof-of-principle validation has been conducted on calcium phosphate glass (CPG)-based bioresorbable optical fibers to assess their capability to monitor the spatial distribution of photosensitizing (PS) drugs in tumors—an essential parameter to optimize for enhanced treatment outcomes in photodynamic therapy (PDT).

Approach: *Ex vivo* validation was performed on liquid phantoms with solid tumor-mimicking inclusions containing the fluorescent PS drug. In-house developed bioresorbable fibers, with optical characteristics similar to silica fibers used in current PDT systems, were utilized. For the first time, these fibers were used for the interstitial acquisition of fluorescent signals, followed by the tomographic reconstruction of the drug distribution in the phantom. The results were compared with those obtained from a standard clinical system equipped with silica fibers.

Results: The reconstructed drug distribution with bioresorbable fibers agreed with that obtained using the same system with standard silica fibers.

Conclusions: We reveal the potential of further exploring CPG bioresorbable optical fibers for interstitial PDT.

© The Authors. Published by SPIE under a Creative Commons Attribution 4.0 International License. Distribution or reproduction of this work in whole or in part requires full attribution of the original publication, including its DOI. [DOI: [10.1117/1.JBO.30.5.058001](https://doi.org/10.1117/1.JBO.30.5.058001)]

Keywords: photodynamic therapy; bioresorbable photonics; photosensitizer distribution; optical fibers; diffuse optical tomography; fluorescence

Paper 240385GR received Dec. 19, 2024; revised Mar. 8, 2025; accepted Apr. 15, 2025; published May 14, 2025.

*Address all correspondence to Stefan Šušnjar, stefan.susnjar@fysik.lth.se

[†]These authors contributed equally to this work.

1 Introduction

Photodynamic therapy (PDT) is a promising cancer treatment modality that involves administering a photosensitizing (PS) drug either topically or intravenously, followed by irradiation of the light at a wavelength that aligns with the PS's absorbance band. In the presence of oxygen, this initiates a cascade of events leading to direct tumor cell death, damage to the tumor's microvasculature, and the activation of a localized inflammatory response.¹⁻³ The effectiveness of PDT depends on a combination of parameters^{2,4} including the type and dose of the PS, the timing between its administration and light exposure, knowledge of the distribution of PS within the tumor, tumor oxygen levels, total light dose, and fluence rate and PDT-induced blood flow changes.^{5,6} There is a growing interest in developing integrated systems that allow real-time interstitial monitoring of these parameters during PDT.⁷⁻⁹ These systems are designed to enable real-time fluence modulation, delivering a more uniform dose to the tumor and improving treatment precision and outcomes. Such advancements are expected to enhance the performance of current clinical interstitial PDT systems, which remain underutilized in clinical practice despite being the first Food and Drug Administration (FDA)-approved drug-device combination in the 1990s.¹⁰

Fiber optic technology is widely used for endoscopic and interstitial light delivery in PDT, enabling the treatment of deep-seated tumors and internal organs.¹¹ In clinical practice, silica-based fiber-optic endoscopy is a well-established method for guiding light. Nevertheless, these endoscopes are inserted only during the procedure and are not suitable for extended monitoring.¹² A major limitation of traditional silica-based fibers is their non-degradable nature, requiring surgical removal after treatment. This not only increases the risk of infection, fibrosis, and procedural complications but also poses a significant challenge in delicate, high-risk environments such as the brain.¹³⁻¹⁵ In multi-session PDT, the repeated insertion and removal of fibers exacerbate patient discomfort, procedural risks, and clinical workload.¹⁴

The motivation for this study stems from the clinical need for precise, minimally invasive, and self-dissolving light delivery and real-time monitoring systems for interstitial PDT, particularly for the treatment of deep-seated and surgically inoperable tumors such as glioblastoma, head and neck, or intra-abdominal tumors.^{16,17} An ideal interstitial PDT tool for such scenarios should efficiently deliver light to deep tumor tissues while naturally degrading post-treatment, eliminating the need for removal, enabling real-time dosimetry to ensure uniform and effective light exposure, and allowing minimally invasive monitoring of drug distribution to optimize therapeutic outcomes. With the development of novel biocompatible and degradable optical fibers for interstitial PDT applications, new therapeutic tools are becoming possible.^{18,19} Relevantly, bioresorbable optical fibers based on calcium phosphate glass (CPG) meet these criteria by combining bioresorbability, optical efficiency, and functional integration.²⁰ Their composition mimics bone minerals, ensuring biocompatibility. They dissolve in physiological media over a clinically relevant time, bypassing the necessity of extraction procedures.^{21,22} Their optical properties can be tailored based on the composition. To the best of our knowledge, CPG fibers possess the lowest optical loss in the category of biocompatible and degradable optical fibers reported in the literature.²³ Along with light delivery, they possess the potential for extended and real-time monitoring of relevant physiological signals, tissue characteristics, or biochemical information.²⁴

CPG-based low-loss optical fibers were first developed using a fiber drawing technique in 2016 by Ceci-Ginistrelli et al.²⁰ Since then, they have been extensively studied for their *in vitro* solubility,²⁵ biocompatibility, and mechanical properties.²⁶ Systematic investigations into their degradation behavior have demonstrated complete dissolution within 1 month, with less than 10% variation in optical power transmission during the first 2 weeks of fiber dissolution.²⁵ In a study by Podrazký et al.,²⁷ mice subcutaneously implanted with CPG fibers showed no clinical signs of adverse effects for up to 5 weeks. CPG fibers possess good thermomechanical properties and have also been recently validated for diffuse optical techniques such as diffuse optical spectroscopy (DOS)²⁸ and diffuse correlation spectroscopy (DCS)²⁹ for monitoring complementary physiological parameters, paving the way for interstitial continuous monitoring of tissue oxygenation, hemodynamics, and metabolism. Despite their benefits, CPG fibers have not been explored for interstitial PDT application.

This study investigates the potential of CPG fibers for light delivery and monitoring in interstitial PDT. Specifically, our objective was to assess whether these fibers could be used

to accurately map the spatial distribution of PS drugs within tumor-mimicking solid phantom inclusions using diffuse fluorescence tomography (DFT). We utilized custom-fabricated multi-mode (MM) CPG fibers along with a well-tested solid-liquid phantom approach.³⁰ The performance of CPG fibers was evaluated against standard silica fibers in terms of their ability to map the PS distribution within the phantoms. This novel approach represents a step toward a minimally invasive therapeutic device that would reduce patient burden and improve the treatment efficacy of deep-seated tumors.

2 Materials and Methods

2.1 CPG Fiber Fabrication

MM bioresorbable CPG optical fiber employed in this study was fabricated through a rod-in-tube technique using an in-house developed drawing tower.²⁰ The glasses for the fiber were made by conventional melt quenching method using high-purity biocompatible chemicals ($\text{P}_2\text{O}_5 \cdot \text{CaO} \cdot \text{Na}_2\text{O} \cdot \text{SiO}_2 \cdot \text{MgO}$). The wavelength-dependent refractive index $n(\lambda)$ of the core (n_{core}) and cladding (n_{cladd}) glasses were then measured at different wavelengths (633, 825, 1061, 1312, and 1533 nm) using a Metricon 2010 prism coupler (Metricon Corporation, United States), with an estimated error of ± 0.0005 . The refractive index values at the wavelength 690 nm (i.e., the wavelength used in DFT experiments reported here, see Sec. 2.2) were then obtained through interpolation using Cauchy's equation. These values were $n_{\text{core}} = 1.5323$ and $n_{\text{cladd}} = 1.5135$. The refractive index difference in core and cladding glass was attained through increasing MgO molar content in the core glass as a substitute for CaO, as detailed in the work by Ceci-Ginistrelli et al.²⁰ The numerical aperture (NA) of the CPG fiber was calculated as $\text{NA} = \sqrt{n_{\text{core}}^2 - n_{\text{cladd}}^2} = 0.24$. This value of NA for CPG fibers is close to the $\text{NA} = 0.22$ of standard silica fibers (Spc Sterile Bare Fiber UVH 400 N SC, LightGuideOptics International Ltd., Germany) employed in clinical PDT systems.

The preform of the fiber consists of a core rod obtained by casting the melt into a 12-mm-diameter cylindrical mold, and a cladding tube with a 10.7-mm outer diameter, realized through an in-house extrusion facility.³¹ The core rod was then stretched to 5.4-mm diameter to fit into the cladding tube. The stretched rod was inserted in the cladding tube and the rod-in-tube preform was further stretched into several 1-m fiber sections using the fiber drawing tower. Optical microscopy (Nikon ECLIPSE E 50i, Nikon Instruments Inc., United States) equipped with the image analysis software ToupView (ToupTek Photonics, China) was used to measure the fiber diameter at the fiber's cross-section. The measured core diameter of the CPG fiber closely matches the diameter of the standard silica fiber (400 μm). The details about the fabrication can be found in previous publications.^{20,31}

For practical experimental convenience, the fabricated fibers were cleaved (CT-106, Fujikura, Japan) into 11 sections of 25 cm each (see Sec. 2.3), which were SMA connectorized at one end by following the protocol for the connectorization of optical fibers.³²

2.2 Phantom Preparation

Tissue-mimicking phantoms with tumorous inclusions were realized. A well-tested hybrid solid-liquid phantom approach based on our previously reported work was followed.³⁰ Briefly, the gelatin-based solid inclusion phantom representing the tumor was submerged in a liquid intralipid-based phantom. Two inclusions, one spherical (volume of 0.6 cm^3) and one ellipsoidal (volume of 3.2 cm^3), were made and stored for later use. These inclusions contained fluorescent photosensitizer verteporfin, an active substance of the PS drug Visudyne (Cheplapharm Arzneimittel GmbH, Germany). A 0.67 mg/kg fluorophore concentration (in milligrams) per phantom mass (in kilograms) was maintained in both inclusions. Following the referenced work by Ghauri et al.,³⁰ the optical properties targeted for the solid phantom inclusion (mixture of gelatin, water, intralipid, and India ink) at 690 nm were absorption $\mu_{ai} = 0.20 \text{ cm}^{-1}$ and reduced scattering coefficient $\mu_{si}' = 15.7 \text{ cm}^{-1}$, mimicking the optical properties of the tumorous region.

Intralipid-based liquid phantom, mimicking surrounding tissue, was prepared by mixing 4.9 ml of 1% India ink solution (Rotring, Germany) and 35.4 ml of intralipid 20% (Fresenius Kabi, Ltd., Germany) in 960 ml of purified water in a glass beaker, which was placed on a magnetic stirrer for mixing. The recipe was chosen to have the optical properties of absorption

$\mu_{abg} = 0.30 \text{ cm}^{-1}$ and reduced scattering $\mu_{sbg}' = 8.3 \text{ cm}^{-1}$ at 690 nm. Each of the gelatin phantoms stored in the freezer at -18°C was taken out and kept for a sufficient time (around 45 min) at room temperature, to bring it toward a thermodynamic equilibrium with the environment and attain mechanical properties convenient for inserting the fibers within inclusion during the measurement (see Sec. 2.3).

2.3 Experimental Setup and Measurements

The phantoms and fiber assembly is shown in Fig. 1(a). Two sets of 11 optical fibers each, one with CPG, and the other with standard silica fibers, were used for the measurements. All 11 CPG fibers from the first set were inserted through a fixed brachytherapy template and positioned within $2 \text{ cm} \times 2 \text{ cm}$ area of the template [Fig. 1(b)]. This number of fibers was chosen to have enough spatial sensitivity to reconstruct the inclusion and background³³ while not complicating the setup with a dense distribution of fibers.

The glass beaker of 10 cm inner diameter, containing 1 l of the liquid phantom, was placed on a lab jack, under the brachytherapy template. Gelatin-based tumor-mimicking spherical solid inclusion was fixed at the CPG fiber tips [see Fig. 1(c)], in the first measurement configuration. The lab jack was vertically adjusted so that the center of the solid tumor-mimicking inclusion was immersed in the liquid at a depth of 7.5 cm from the surface, and height of 5.5 cm from the bottom [Fig. 1(c)]. In the second measurement configuration, the spherical inclusion was replaced by the ellipsoidal one, within the same liquid phantom. In the case of the spherical inclusion, two fiber tips were within the inclusion, whereas in the case of the ellipsoidal, five fiber tips were within the inclusion [see Fig. 1(b)].

The same experimental procedure was then repeated with the set of silica fibers instead of CPG fibers, inserted at the same 11 positions in the brachytherapy template as before. The same

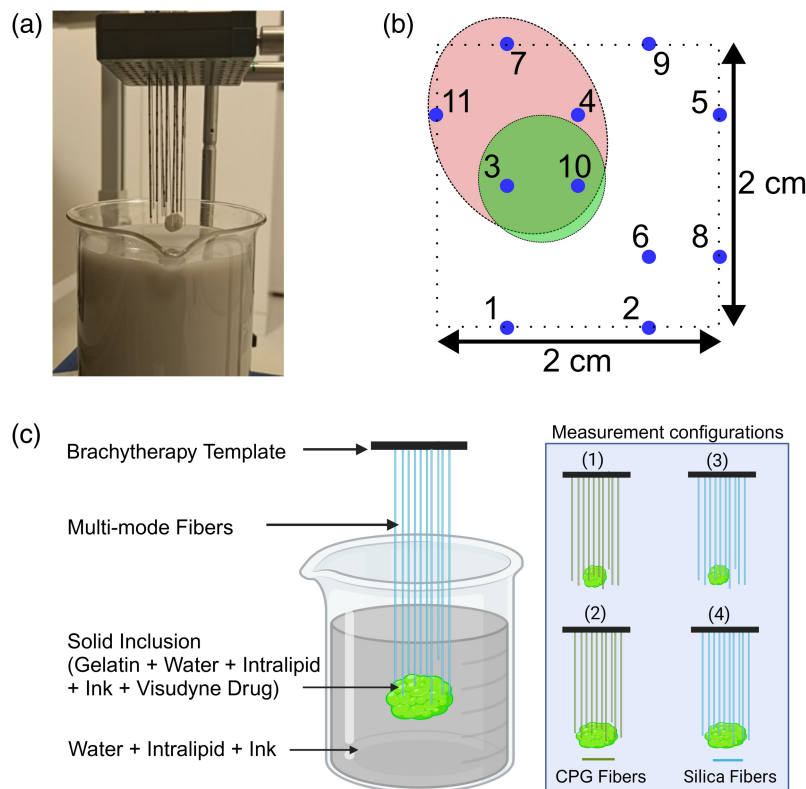


Fig. 1 (a) Experimental setup with CPG fibers, liquid tissue-mimicking phantom, and solid gelatin-based tumor-mimicking fluorescent inclusion, before the measurement. (b) Schematic showing the fiber positioning within the inclusions—spherical (green) and ellipsoidal (red)—where the blue markings represent the 11 fiber centers in the plane (horizontal) parallel to the brachytherapy template. (c) Schematic representing the hybrid phantom and fibers assembly during the measurement (left), along with the simplified schematics of all four measurement configurations (right).

Table 1 Details of the measurements conducted including the types of fibers used, the shape of the inclusion, and the protocol followed during each acquisition cycle.

| | Fiber type | Inclusion shape | Protocol in one measurement cycle |
|---|------------|-----------------|--|
| 1 | CPG | Sphere | Light delivery from PM1 through fiber 1 and simultaneous light collection by fibers 2–11 (~3 s). |
| 2 | | Ellipsoid | |
| 3 | Silica | Sphere | Switching the light delivery sequentially from PM1 to PM11, with subsequent light collection by all other fibers before each switch. |
| 4 | | Ellipsoid | |
| | | | Acquisition of $11 \times 10 = 110$ data points. |

liquid phantom, and the same solid inclusions as in the first two measurement configurations were used. The spherical one was used in the third configuration and placed at the same position as in the first, whereas the ellipsoidal one was used in the fourth configuration and placed at the same position as in the second [Fig. 1(c)].

During the measurements, PDT-like light delivery was conducted using SpectraCure's P18 system comprising 18 photonics modules (PMs) to which the optical fibers can be connected. Each PM is capable of delivering light at 690 nm (Laser diode LDX-2405-690, LDX Optronics Inc., United States) and detecting (Si photodiode S12915-5K, Hamamatsu Photonics, Japan) both light around that excitation wavelength as well as fluorescent light at longer wavelengths (>700 nm). Two-meter-long silica fibers and 25-cm-long CPG fibers (SMA connectorized) were connected to SC ports in the P18 system via 45-cm SC-SMA patch cables. The choice of this rationale for using shorter sections of CPG fibers is based on the possible future clinical implantation, where long fibers are not required.³⁴ The PMs were calibrated to deliver 170 mW at the output of the SC-SMA patch cable, in accordance with the system specifications.

A complete measurement consists of five cycles. Each measurement cycle involves continuous light delivery from one fiber during a particular time interval while all the other fibers detect this excitation and fluorescence emission light. The cycle is continued by the other fibers sequentially delivering light, one after another (see Table 1). The light delivery from each fiber lasted ~3 s followed by a delay of 0.1 s for shifting the light delivery to the next fiber. The 3 s light delivery per fiber was long enough to reliably measure excitation and fluorescent light without causing photobleaching of the PS due to longer exposure time.³⁰ The measurement data points are obtained by taking the average from all five cycles. Before each measurement, the setup was covered with a dark, light-proof curtain. The summary of all the measurements is given in Table 1.

2.4 Data Processing and Reconstruction

Data collected from tomographic measurements were first processed such that the fluorescent signals below the defined threshold $P_{th} = 5.4 \cdot 10^{-11}$ W were set to zero, and all other fluorescent signals were reduced by the same threshold value P_{th} . This was done to remove the effect from unreliable data points (where the signal is too low compared with the measurement uncertainties), in a way similar to our previous work.³³ The tomographic reconstruction algorithm used here was reported previously.³³ Briefly, 110 data points (all source-detector fiber pairs from 11 fibers), represented as Born ratios between the detected power of fluorescent light (wavelengths >700 nm) and the detected power at the excitation wavelength (690 nm), were given as input to the reconstruction algorithm. The inhomogeneous medium of $(5.0 \times 5.0 \times 3.8)$ cm³ was divided into a finite element mesh of $N_e = 97,906$ tetrahedrons with $N_n = 21,616$ nodes. The computer implementation was done using MATLAB (The Mathworks Inc., 2022) and the NIRFAST package.^{35,36} The reconstruction consists of calculating the forward model for every source-detector pair and solving the inverse problem by iteratively updating the estimates for the fluorescent yields in mesh nodes to minimize the discrepancy between the forward model vector \mathbf{F} and the measurement data vector \mathbf{M} . For a given vector of fluorescent yields in all nodes $\boldsymbol{\eta} = (\eta_1, \eta_2, \dots, \eta_{N_n})$ and for a specific source-detector pair (s, d) , the Born ratio from the forward model is^{1,33}

$$F_{s,d}(\boldsymbol{\eta}) = \frac{1}{G_x(\vec{r}_d, \vec{r}_s)} \sum_{i=1}^{N_n} G_x(\vec{r}_i, \vec{r}_s) G_m(\vec{r}_i, \vec{r}_d) \eta_i \Delta V, \quad (1)$$

where ΔV is the element volume, η_i is the fluorescent yield in node i (at the position \vec{r}_i), \vec{r}_s and \vec{r}_d are positions of the source and the detector, respectively, and G_x and G_m are Green's functions solutions at the excitation and fluorescent emission wavelengths, respectively.³³

The inverse problem is solved in two stages, referred to as S1 and S2. In S1, because the problem is ill-posed (the number of unknowns (nodes) is much greater than the number of measurement data points), the goal is to minimize the Tikhonov regularization cost function^{1,33}

$$\Omega(\boldsymbol{\eta}) = \|\mathbf{M} - \mathbf{F}(\boldsymbol{\eta})\|^2 + \lambda \|\mathbf{L}(\boldsymbol{\eta} - \boldsymbol{\eta}_0)\|^2, \quad (2)$$

where λ is the regularization parameter, \mathbf{L} is the regularization matrix, $\boldsymbol{\eta}_0$ is the initial estimate for the vector of unknowns $\boldsymbol{\eta}$, and $\|x\|$ denotes Euclidean two-norm of vector x . The modification of the Levenberg-Marquardt algorithm was used to calculate the updates for fluorescent yield estimates according to³³

$$\boldsymbol{\eta}_{i+1} = \boldsymbol{\eta}_i + (\mathbf{J}_i^T \mathbf{J}_i + \lambda_i \mathbf{L}^T \mathbf{L})^{-1} \mathbf{J}_i^T \boldsymbol{\delta}(\boldsymbol{\eta}_i), \quad (3)$$

where indices i and $i+1$ denote the ordinal number of the iteration and matrix $\mathbf{J} = \frac{\partial \mathbf{F}(\boldsymbol{\eta})}{\partial \boldsymbol{\eta}}$ is the Jacobian of the system. The regularization parameter λ is initialized to the maximum of the diagonal of the Hessian matrix: $\lambda_0 = \max\{\text{diag}(\mathbf{J}_0^T \mathbf{J}_0)\}$ and updated in every iteration to $\lambda_i = \max\{\text{diag}(\mathbf{J}_i^T \mathbf{J}_i)\} \cdot 10^{-i/4}$. The regularization matrix \mathbf{L} was set to an identity matrix, so as not to bias the solution with *a priori* information about the geometry. The reconstructed fluorescent yield $\boldsymbol{\eta}$ is transformed to the fluorophore absorption μ_{af} using the relation $\boldsymbol{\eta} = \gamma \mu_{af}$ and assuming homogeneous quantum efficiency of $\gamma = 10\%$,^{37,38} for fluorescence emission by verteporfin.

S2 of the reconstruction is described in our previous work³³ and assumes the number of unknowns (originally the number of nodes N_n) is reduced to the number of regions (N_r) with homogeneous fluorescent yield. The regions are defined according to the results from S1. The introduction of S2 improves the accuracy of the solution with respect to S1,³³ which is necessary for the quantitative performance comparison between CPG and standard silica fibers. The fluorescent yield estimate updates in S2 are still calculated according to Eq. (3), but without the regularization and with the reduced size of the Jacobian and the vector of unknowns.³³ The iterative method stops when the relative decrease of the two-norm of the difference between the forward model and the measurements vector is $<2\%$, or the maximal number of iterations is reached.³⁶

3 Results

The results of DFT reconstruction from phantom measurements with silica and CPG fibers are shown in Fig. 2. The first two columns compare the performance of silica fibers (a) and CPG fibers (b) in retrieving the PS distribution in the phantom with the spherical tumor-mimicking inclusion. Columns (c) and (d) compare the performance of silica and CPG fibers, respectively, for the measurements with the ellipsoidal tumor-mimicking inclusion. The results shown in the first row (from above) are from S1, whereas the second row corresponds to the results from S2 (Sec. 2.4). The quantified fluorophore absorption and estimated volume of the inclusion obtained in S2 are also indicated in Fig. 2.

Considering the case of the spherical inclusion with the fluorescent PS drug inside, we do not observe any significant difference in the reconstructed fluorophore absorption values obtained using silica fibers and CPG fibers [Figs. 2(a) and 2(b)]. Similar can be said for the case of the ellipsoidal inclusion [Figs. 2(c) and 2(d)]. However, the reconstructed values for the fluorophore absorption coefficient are slightly different for spherical and ellipsoidal inclusions. The reconstructed volume is underestimated in all cases, for spherical and ellipsoidal inclusions. The true volume of the sphere was around 0.6 cm^3 and of the ellipsoid around 3.2 cm^3 . The underestimation of the reconstructed volume leads to overestimating the reconstructed absorption,³³ as discussed in Sec. 4. The reconstructed fluorophore absorption coefficients are

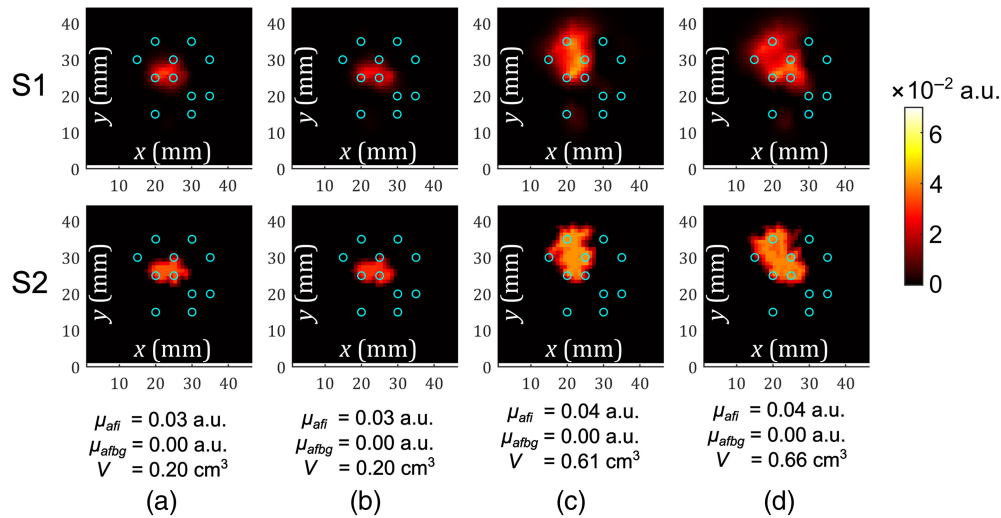


Fig. 2 Tomographic reconstruction results for the measurements with (a) spherical inclusion and silica fibers, (b) spherical inclusion and CPG fibers, (c) ellipsoidal inclusion and silica fibers, and (d) ellipsoidal inclusion and CPG fibers. Slices through the planes cutting the inclusion in halves. Resulting fluorophore absorption (originating from PS) coefficients 2D color map in the first stage (S1) and in the second stage (S2) of the reconstruction shown in different rows. Numerical values for the reconstructed fluorophore absorption coefficients of the inclusion μ_{afj} and the background μ_{afbg} , as well as the estimated volume of the inclusion V given below. Blue circles represent fiber projections in the xy -plane.

more overestimated in the case of ellipsoidal inclusion compared with spherical inclusion because the volume of the reconstructed ellipsoid is more underestimated compared with the reconstructed sphere. When the reconstructed volumes are relatively close, as in Figs. 2(a) and 2(b), and Figs. 2(c) and 2(d), the reconstructed fluorophore absorption coefficients can be compared with each other.³³ This implies that CPG and silica fibers performed similarly in DFT reconstructions from our measurements, demonstrating the potential of bioresorbable CPG fibers to monitor the distribution of PS drugs in PDT.

4 Discussion

The aim of this study was to determine the PS spatial distribution monitoring capabilities of CPG fibers within tissue-mimicking phantoms using DFT. The relative comparison between silica and CPG fibers showed good alignment in the reconstructed values for the fluorophore absorption coefficient and the volume of the tumor-mimicking inclusions. The two inclusions with different volumes and shapes were chosen to assess the potential of DFT for monitoring PS distribution regardless of tumor size and morphology. The absolute values for the volume are different from what was expected (the reconstructed volume is underestimated around 3 to 5 times with respect to the ground truth), hence also the absorption.

This volume underestimation was mainly due to the measurement data processing employed here, which is modified from our previous work.³³ The present approach was chosen to trade off the optical power variation among CPG fibers. This power variation could have originated from the process of their in-house connectorization, where the bore size of the available standard SMA connectors (1040 μm) was greater than the diameter of the CPG fiber (870 μm). This might have caused a slight misalignment of the fiber from the central axis of the ferrule. As a consequence, along with CPG material losses,²⁰ the power available at the fiber tip (in the tissue phantom) ranged 75 to 85 mW in different CPG fibers, compared with 150 mW obtained at the silica fiber tips. The variation in optical power among CPG fibers can be reduced by professional connectorization methods.

Because the use of the Born ratio (see Sec. 2.4) helps in canceling out many uncertainties regarding the fiber output and collected powers, there were no significant differences between the reconstructions with silica and CPG fibers. However, for a robust convergence to a solution of

an inverse problem in all the considered cases (both with silica and CPG fibers), a certain level of signal corresponding to the estimated level of noise threshold (Sec. 2.4) had to be subtracted from every measurement data point, causing the volume underestimation.

As stated in our previous work,³³ reconstruction results are sensitive to the true fiber positions, as well as the optical properties of the phantom. In our experiments, the information on the true fiber tip positions was not available once inserted into the phantom. Therefore, it was difficult to achieve exactly the same fiber and inclusion positioning in all four measurement configurations with different fiber types and inclusion shapes. Consequently, small quantitative differences between the reconstructions from the measurements with silica and CPG fibers were expected. It should be noted that the information on the fiber positioning as well as the estimated optical properties of tissue is already available in the clinical setting.^{39,40} Applying similar methods for estimating the implanted CPG fiber positions in future trials could pave the way for more reliable reconstruction.

Overall, in this first test of CPG fibers for DFT in PDT, we observed that there was no significant difference in the reconstruction results obtained from the tomographic measurements with silica and CPG fibers. It should be noted that this test model, comprised of SpectraCure's P18 system for interstitial PDT and phantoms with PS verteporfin, was chosen because it was readily available for a proof-of-principle demonstration. Although the P18 system is currently applied in interstitial PDT of prostate cancer, there is no limitation to follow the same concept and generalize this system for PDT of other internal tumors, such as glioblastoma, where bioresorbable fibers would be highly desirable and better choice than standard non-degradable fibers.

This study establishes the foundation for an interesting perspective in extended interstitial monitoring of PS concentration with implantable bioresorbable fibers and can have positive implications for planning, optimizing, and predicting or monitoring treatment outcomes.⁴¹ Moreover, the concept of implantable optical fibers and implantation procedures has previously been validated with silica MM fibers in mice for long-term monitoring in optogenetic applications.³⁴ Combining DFT with other diffuse optical modalities such as DOS and DCS in the future, for which the bioresorbable fibers have been previously validated,^{28,29} within a single bioresorbable platform could provide information about the complementary physiological and biochemical signals, which will find significant insights in enhancing the interstitial therapeutic outcomes.

5 Conclusion

In this study, we have proposed for the first time the use of bioresorbable optical fibers for DFT in PDT of tumors. By detecting the fluorescent light originating from the PS drug, the spatial distribution of the drug was estimated using the CPG fibers within phantoms with tumor-mimicking inclusions. The results demonstrated good agreement compared with the PDT system equipped with standard silica fibers, in both spherical and ellipsoidal inclusions. The demonstrated concept of monitoring PS distribution in PDT using CPG fibers marks a step forward in the development of an implantable and resorbable multifunctional theranostic platform. Further exploration should focus on extended monitoring with fiber degradation, followed by *in vivo* validation.

Disclosures

JS is a minority shareholder of SpectraCure AB and is interested in prostate cancer interstitial photodynamic therapy. SKVS is a shareholder of BioPixS Ltd with an interest in tissue optical phantoms.

Code and Data Availability

Data underlying the results presented in this paper are not publicly available at this time but may be obtained from the authors upon reasonable request.

Acknowledgments

This project was funded by the EU H2020 MSCA-ITN project "Photonics for Healthcare: multiscale cancer diagnosis and therapy" (PHAST-ETN) (Grant No. 860185).

References

1. J. Axelsson, J. Swartling, and S. Andersson-Engels, "In vivo photosensitizer tomography inside the human prostate," *Opt. Lett.* **34**, 232–234 (2009).
2. P. Agostinis et al., "Photodynamic therapy of cancer: an update," *Cancer J. Clin.* **61**(4), 250–281 (2011).
3. J. F. Algorri et al., "Photodynamic therapy: a compendium of latest reviews," *Cancers* **13**(17), 4447 (2021).
4. M. M. Kim and A. Darafsheh, "Light sources and dosimetry techniques for photodynamic therapy," *Photochem. Photobiol.* **96**(2), 280–294 (2020).
5. D. van Straten et al., "Oncologic photodynamic therapy: basic principles, current clinical status and future directions," *Cancers* **9**(2), 19 (2017).
6. J. D. Vollet-Filho et al., "Non-homogeneous liver distribution of photosensitizer and its consequence for photodynamic therapy outcome," *Photodiagn. Photodyn. Ther.* **7**(3), 189–200 (2010).
7. T. C. Zhu, J. C. Finlay, and S. M. Hahn, "Determination of the distribution of light, optical properties, drug concentration, and tissue oxygenation in-vivo in human prostate during motexafin lutetium-mediated photodynamic therapy," *J. Photochem. Photobiol. B: Biol.* **79**(3), 231–241 (2005).
8. J. H. Woodhams, A. J. MacRobert, and S. G. Bown, "The role of oxygen monitoring during photodynamic therapy and its potential for treatment dosimetry," *Photochem. Photobiol. Sci.* **6**(12), 1246–1256 (2007).
9. G. Yu et al., "Real-time in situ monitoring of human prostate photodynamic therapy with diffuse light," *Photochem. Photobiol.* **82**(5), 1279–1284 (2006).
10. G. Gunaydin, M. E. Gedik, and S. Ayan, "Photodynamic therapy for the treatment and diagnosis of cancer—a review of the current clinical status," *Front. Chem.* **9**, 686303 (2021).
11. T. S. Mang, "Lasers and light sources for PDT: past, present and future," *Photodiagn. Photodyn. Ther.* **1**(1), 43–48 (2004).
12. J. M. H. Bergein, F. Overholt, and M. Panjehpour, "Photodynamic therapy for Barrett's esophagus: follow-up in 100 patients," *Gastrointest. Endosc.* **49**(1), 1–7 (1999).
13. D. Wang et al., "Phototherapy and optical waveguides for the treatment of infection," *Adv. Drug Deliv. Rev.* **179**, 114036 (2021).
14. R. Nazempour et al., "Emerging applications of optical fiber-based devices for brain research," *Adv. Fiber Mater.* **4**, 24–42 (2021).
15. P. Abdollahian et al., "In vivo evaluation of thermally drawn biodegradable optical fibers as brain implants," *J. Biomed. Mater. Res. Part B: Appl. Biomater.* **113**, e35549 (2025).
16. S. Cramer and C. Chen, "Photodynamic therapy for the treatment of glioblastoma," *Front. Surg.* **6**, 81 (2020).
17. S. H. Mussavi Rizi et al., "Phosphate glass-based microstructured optical fibers with hole and core for biomedical applications," *Opt. Mater.* **131**, 112644 (2022).
18. Y. Hu et al., "Fiber optic devices for diagnostics and therapy in photomedicine," *Adv. Opt. Mater.* **12**(22), 2400478 (2024).
19. W. Pang et al., "Biocompatible polymer optical fiber with a strongly scattering spherical end for interstitial photodynamic therapy," *Opt. Lett.* **48**, 3849–3852 (2023).
20. E. Ceci-Ginistrelli et al., "Novel biocompatible and resorbable UV-transparent phosphate glass based optical fiber," *Opt. Mater. Express* **6**, 2040–2051 (2016).
21. W. Bai et al., "Bioresorbable photonic devices for the spectroscopic characterization of physiological status and neural activity," *Nat. Biomed. Eng.* **3**(8), 644–654 (2019).
22. C. M. Boutry et al., "Towards biodegradable wireless implants," *Philos. Trans. Ser. A, Math. Phys. Eng. Sci.* **370**(1967), 2418–2432 (2012).
23. J. T. Pandayil, N. G. Boetti, and D. Janner, "Advancements in biomedical applications of calcium phosphate glass and glass-based devices—a review," *J. Funct. Biomater.* **15**(3), 79 (2024).
24. X. Wu and Q. Guo, "Bioresorbable photonics: materials, devices and applications," *Photonics* **8**(7), 235 (2021).
25. J. T. Pandayil et al., "Towards a novel bi-functional bioresorbable micro-structured optical fiber for theranostic applications," *Proc. SPIE* **12627**, 126271N (2023).
26. V. M. Sglavo et al., "Mechanical properties of resorbable calcium-phosphate glass optical fiber and capillaries," *J. Alloys Compd.* **778**, 410–417 (2019).
27. O. Podrazký et al., "In vivo testing of a bioresorbable phosphate-based optical fiber," *J. Biophotonics* **12**(7), e201800397 (2019).
28. L. Di Sieno et al., "Towards the use of bioresorbable fibers in time-domain diffuse optics," *J. Biophotonics* **11**(1), e201600275 (2018).
29. J. T. Pandayil et al., "Proof of concept validation of bioresorbable optical fibers for diffuse correlation spectroscopy," *J. Biomed. Opt. Express* **15**(11), 6384–6398 (2024).
30. M. D. Ghauri et al., "Hybrid heterogeneous phantoms for biomedical applications: a demonstration to dosimetry validation," *Biomed. Opt. Express* **15**, 863–874 (2024).
31. D. Gallichi-Nottiani et al., "Toward the fabrication of extruded microstructured bioresorbable phosphate glass optical fibers," *Int. J. Appl. Glass Sci.* **11**(4), 632–640 (2020).

32. Thorlabs, *FN96A Guide to Connectorization and Polishing of Optical Fibers*, Thorlabs Inc. (2019).
33. S. Šušnjar et al., “Two-stage diffuse fluorescence tomography for monitoring of drug distribution in photodynamic therapy of tumors,” *J. Biomed. Opt.* **30**(1), 015003 (2025).
34. D. R. Sparta et al., “Construction of implantable optical fibers for long-term optogenetic manipulation of neural circuits,” *Nat. Protoc.* **7**, 12–23 (2012).
35. M. Jermyn et al., “Fast segmentation and high-quality three-dimensional volume mesh creation from medical images for diffuse optical tomography,” *J. Biomed. Opt.* **18**(8), 086007 (2013).
36. H. Dehghani et al., “Near infrared optical tomography using NIRFAST: algorithm for numerical model and image reconstruction,” *Commun. Numer. Methods Eng.* **25**(6), 711–732 (2009).
37. T. Monahan, S. Jiang, and B. Pogue, “Fluorescence quantum yield of verteporfin is independent of oxygen,” *Proc. SPIE* **6845**, 684517 (2008).
38. B. M. Aveline, T. Hasan, and R. W. Redmond, “The effects of aggregation, protein binding and cellular incorporation on the photophysical properties of benzoporphyrin derivative monoacid ring A (BPDMA),” *J. Photochem. Photobiol. B: Biol.* **30**(2), 161–169 (1995).
39. J. Swartling et al., “System for interstitial photodynamic therapy with online dosimetry: first clinical experiences of prostate cancer,” *J. Biomed. Opt.* **15**(5), 058003 (2010).
40. A. Johansson et al., “Realtime light dosimetry software tools for interstitial photodynamic therapy of the human prostate,” *Med. Phys.* **34**(11), 4309–4321 (2007).
41. T. Busch, “Local physiological changes during photodynamic therapy,” *Lasers Surg. Med.* **38**(5), 494–499 (2006).

Jawad T. Pandayil is currently a PhD student in the Department of Material Sciences and Technology (DISAT) in Politecnico di Torino. At LINKS Foundation, he is an early-stage researcher within the European Training Network PHAST (Photonics for Healthcare: multiscale cancer diagnosis and Therapy), working on the development of multifunctional resorbable optical fibers for theranostics applications. He received his 5-year-integrated master’s degree in photonics from CUSAT, Kerala, India. His research interests are currently focused on biophotonics and biomaterials, fiber optics, and laser spectroscopy.

Stefan Šušnjar is a PhD student at the Department of Physics, Lund University, Sweden, and an early-stage researcher at SpectraCure AB. Stefan completed his BS degree in electrical engineering and computing, in 2018, at the University of Belgrade, Serbia. He completed his MS degree in engineering physics, in 2020, at Politecnico di Milano, Italy, and received his double MS degree from “Alta Scuola Politecnica.” His current research interest is the application of photonics in medical diagnostics and treatments.

Muhammad Daniyal Ghauri is an early-stage researcher in Biophotonics@Tyndall, Tyndall National Institute, Ireland. He received his BSc in electrical and electronic engineering from the University of Bradford, UK, in 2016, and his MSc in electrical engineering from the Lahore University of Management Sciences (LUMS), Pakistan, in 2019. His current research interests include the use of optical technologies for therapeutic applications.

Sanathana Konugolu Venkata Sekar is a leading scientist and entrepreneur with over a decade of experience in biophotonics and is a recipient of an ERC grant. He leads the Integrated Fast Biophotonics Group, where he co-supervises a team of eight PhDs and two postdoctoral researchers. In addition, he co-founded BioPixS Ltd, a spinoff of his research. His key areas of interest include phantoms and standardization, time-domain diffuse optics, pulse oximeters, FLIM, endoscopes, multimodal microscopy, and probes. His vision is to translate cutting-edge photonics into miniaturized solutions for healthcare applications.

Johannes Swartling holds a PhD in physics from Lund University (2002). He has worked with product development and general management in the medical device company SpectraCure AB and other companies since 2006. Before joining SpectraCure AB, he held post-doctoral research positions at Politecnico di Milano, Italy, and at Cambridge University, UK. His research has been on applications of laser technology and spectroscopy in biology and medicine. He currently serves as CTO at SpectraCure AB.

Davide Janner is currently an associate professor in the Department of Material Sciences and Technology (DISAT) at Politecnico di Torino. He received his PhD in physics from Politecnico di Milano in 2006 and his MSc degree in physics from Università degli Studi di Milano, Milan

(Italy), in 2002. His research interests are currently focused on glass materials for photonics applications, photonic sensors, and micro-/nano-structured multifunctional materials. He has published more than 120 papers in international peer-reviewed journals, gave 11 invited talks at major international conferences, and has four granted patents.

Nadia G. Boetti is a technology specialist in optical devices and materials at LINKS Foundation, Italy. She holds an MSc degree with honors in physics from the University of Torino and a PhD in electronic devices from Politecnico di Torino. Her current research activities deal mainly with the design, fabrication, and characterization of photonic glasses and optical fibers for lasers and amplifiers in the visible, near-infrared, and mid-infrared wavelength regions. She is involved in the development of bioresorbable glasses, optical fibers, and capillaries for biophotonic applications. She has published more than 115 works, including 44 papers in international peer-reviewed journals and three book chapters.

Nina Reistad is an associate professor at the Department of Physics at the Faculty of Engineering, Lund University, Sweden. The main topic during her PhD studies was spectroscopy, and she received her PhD in physics from Lund University in 1987, followed by a docentship in 1993. 2009 she was recognized as an excellent teaching practitioner (ETP). She is one of the researchers within the research profile areas “engineering health” and “photon science and technology” at the Faculty of Engineering, “Light and Materials” at Lund University, and also a researcher at Lund University Cancer Centre (LUCC). Her current research interests include tissue-mimicking materials and various optical techniques for tissue diagnostics and imaging.